Structure and viscoelastic properties of hybrid ferrogels with iron oxide nanoparticles synthesized *in situ*

Rebeca Hernández,[*a] Javier Sacristán,[a] Aurora Nogales,[b] Manuel Fernández,[c] Tiberio A. Ezquerra[b] and Carmen Mijangos[a]

Ultra small angle X-ray scattering (USAXS) experiments in the q-range (10^{-4}–0.2 Å) were performed to determine the structure of iron oxide NPs *in situ* synthesized inside semi-interpenetrating polymer networks (semi-IPNs) of linear alginate and crosslinked poly(*N*-isopropylacrylamide) (PNiPAAm). Results from the fitting of USAXS experiments were related with the reinforcement and swelling properties exhibited by the hybrid semi-IPNs which, in turn, were found to be highly dependant on the alginate concentration and the volume fraction of iron oxide nanoparticles. The USAXS findings, along with those from rheological and swelling measurements, allow determining whether iron oxide nanoparticles are bonded to the polymer matrix or if they are simply 'packed' inside the polymer network without interaction with the polymer chain.

1. Introduction

The hybrids comprising of inorganic and organic materials have attracted intensive attention lately because of their great versatility and easy fabrication for the demands of modern materials by combining important properties into a single composition system through tuning and tailoring of functionalities.[1,2] The use of polymeric networks as templates for the growth of inorganic nanoparticles constitutes a powerful method to synthesize hybrid materials because polymer organic matrixes provide chemically and spatially confined environments that control the nanoparticles size and their aggregation.[3–8] In this context, it has been demonstrated that hydrogels derived from polysaccharides are effective templates for the *in situ* synthesis of iron oxide NPs. This is mainly because some of them can interact with the iron nanoparticles thus preventing their diffusion into the solution in which the gel is immersed.[9,10] An example of this is alginate, a polysaccharide extracted from brown algae,[11] that has been extensively employed to precipitate iron oxide NPs in order to obtain ferrogels and ferrofluids with response to magnetic fields.[12–14] Ferrogels consisting of iron oxide nanoparticles (NPs) embedded in polymer gels that respond to external magnetic stimuli are increasingly used in biosciences and medicine as hyperthermia agents for cancer therapy or magnetically targeted carriers of drugs.[15–19]

We have recently described a method to obtain ferrogels with response to temperature and magnetic fields, in which the iron oxide NP synthesis is carried out through coprecipitation of iron salts in alkaline solutions inside semi-IPNs constituted of linear alginate and crosslinked poly(*N*-isopropylacrylamide).[20] The loading procedure can be repeated in order to increase the iron oxide NPs volume fraction. It has been demonstrated that the synthesis '*in situ*' of iron oxide NPs in Alg-PNiPAAm semi-IPNs greatly increases the porosity of the resulting semi-IPNs due to the partial hydrolysis of the alginate chains. This facilitates the hydrophobic interactions between the PNiPAAm isopropyl groups thus lowering the lower critical solution temperature (LCST) and improving the deswelling rate of the resulting networks with respect to pure PNiPAAm.

In addition, the synthesis *in situ* of iron oxide NPs inside Alg-PNiPAAm semi-IPNs allows on the one hand controlling the polydispersity of the iron oxide NPs when compared to the reaction carried out in an alginate solution.[20] In this way, the polymeric gel acts as a spatial framework to control the iron oxide NPs size distribution. Besides, the diffusion of the iron oxide NPs out of the Alg-PNiPAAm semi-IPNs is prevented due to the establishment of interactions between the iron oxide NPs and the polymer matrix. However, the nature of these interactions is not well understood. Some studies have reported that both Fe^{2+} and Fe^{3+} can be coordinated to the carboxyl groups in alginate and that such binding may lead to iron-mediated crosslinking of different alginate molecules.[21,22] Another possibility is that the iron oxide NPs are simply 'packed' in the Alg-PNiPAAm semi-IPNs without interaction with the polymer chains. In this study we seek to elucidate the role of the alginate content on the establishment of interactions between the iron oxide NPs and the polymer matrix on the one hand and, on the other hand, on the structural organization of iron oxide NPs synthesized *in situ*. To achieve this aim, we will consider two model series of semi-IPN of alginate and PNiPAAm with two different alginate contents (0.5 and 1 wt%) subjected to a varying number of oxidation cycles (1 to 3). Swelling and rheological measurements will be employed to asses the influence of the iron oxide NPs on the reinforcement of the polymer semiIPNs as well as to determine the presence of interactions between the iron oxide NPs and the polymer matrix. The structural organization of the iron oxide NPs synthesized *in situ* will be carried out through ultra small

[a]Instituto de Ciencia y Tecnología de Polímeros, CSIC, Juan de la Cierva, 3, 28006 Madrid, Spain. E-mail: rhernandez@ictp.csic.es; Fax: +34 91 564 48 53; Tel: +34 91 562 29 00
[b]Instituto de Estructura de la Materia, CSIC, Serrano 119, Madrid, 28006, Spain
[c]ID02, European Synchrotron Radiation Facility, BP 220, 38043 Grenoble, France

X-ray scattering (USAXS) as the main experimental probe to determine the characteristics of aggregates and primary particles using the unified fitting equation.

2. Experimental part

2.1. Materials

N-Isopropylacrylamide (N-AAm), the initiator potassium persulfate, the crosslinker N,N′-methylene bisacrylamide (Bis), ferrous chloride (FeCl₂*4H₂0), ferric chloride (FeCl₃*6H₂O) and alginic acid sodium salt from brown algae (65–70% guluronnic acid and $M_w = 100–200$ K) were all purchased from Aldrich and used as received.

2.2. Synthesis of semi-interpenetrating polymer networks (semi-IPNs)

Semi-interpenetrating polymer networks constituted by linear alginate and crosslinked PNiPAAm were obtained by polymerizing N-AAm (0.65 mol L⁻¹) and Bis in an alginate aqueous solution. Solutions were poured out into Petri dishes and allow reacting at room temperature for 24 h. Two series with the same degree of crosslinking of PNiPAAm (mol$_{BIS}$/mol$_{N-AAm}$ = 3%) and different alginate concentrations were synthesized, series I with 0.5 wt% sodium alginate (Alg0.5-PNiPAAm) (mol$_{alginate}$/mol$_{PNiPAAm}$ = 0.04) and series II with 1 wt% sodium alginate (Alg1-PNiPAAm) (mol$_{alginate}$/mol$_{PNiPAAm}$ = 0.09).

2.3. Synthesis in situ of iron oxide NPs

Cylindrically shaped specimens of 20 mm in diameter were cut from the Alg-PNiPAAm samples and immersed in 200 mL aqueous solution containing 2.1 g FeCl₂*4H₂O and 5.8 g FeCl₃*6H₂O under constant N₂ bubbling during 4 h. After that period of time, yellowish gels were obtained and immersed in a 0.5 M NH₃ (30 wt%) under constant N₂ bubbling during 30 min. The resulting black gels were washed with distilled water for 24 h.

The procedure was repeated up to three times. The resulting gels were designated as FeAlg-PNiPAAm (1c), FeAlg-PNiPAAm (2c) and FeAlg-PNiPAAm (3c) where the numbers in brackets denote the number of oxidation cycles.

The iron oxide NPs volume fraction, Φ_{NPs} can be obtained by employing the density of the magnetite, ρ_{Fe3O4} (ρ_{Fe3O4} = 5.24 g cm⁻³) as an approximation so that:

$$\Phi_{NPs}(\%) = \frac{W_{NPs} \times \rho_f}{\rho_{Fe_3O_4}} \times 100 \qquad (1)$$

where W_{NPs} is the NPs weight fraction obtained from thermogravimetric experiments performed on dried samples where the residual weight at 950 °C was taken as the indication of the iron oxide content.[20] The density of the ferrogels, ρ_f, $\rho_f = (M_{dry} \times \rho_{H_2O})/(M_s - M_{dry})$, was obtained from the weights of the dried gels, M_{dry}, and swollen gels, M_s. The data corresponding to Φ_{NPs} are all reported in Table 1.

Table 1 Volume fraction of the nanoparticles, Φ_{NPs} (%) inside Alg-PNiPAAm semi-IPNs

	Number of oxidation cycles	Φ_{NPs} (%)
Series I (0.5 wt% alginate)	1c	0.15
	2c	0.33
	3c	0.48
Series II (1 wt% alginate)	1c	0.10
	2c	0.16
	3c	0.31

2.4. Swelling measurements

Ferrogels swollen to equilibrium in distilled water were weighed (M_s) and then they were dried at 70 °C and weighed again to obtain the dry mass of the total ferrogel (M_{dry}). The total water content, W_t, was calculated according to the equation:

$$W_t = M_s - M_{dry}/M_{dry} - M_{NPs} \qquad (2)$$

where M_{NPs} is the mass of iron oxide nanoparticles in the ferrogels obtained from thermogravimetric analysis of dried ferrogels.[20]

2.5. Confocal Raman spectroscopy

Raman spectra were collected using a Renishaw InVia reflex Raman microscope. The Raman scattering was excited with a 785 nm near-infrared diode laser. A 100×, NA90 objective lens was used, giving a laser spot diameter of ∼1 μm and the sampling depth is estimated to be around 1.5 μm (half-width of the confocal depth profile for a silicon wafer). In order to avoid thermal decomposition/degradation of the samples, laser intensity at the sample was reduced to 0.5–1%. Spectra were obtained for a 20 s exposure of the CCD detector in the region 100–1800 cm⁻¹ using the extended scanning mode of the instrument and the number of data acquisition cycles that make up the measurement was 2. Raman spectra, were recorded and subsequently analysed by using Wire software (Renishaw).

2.6. Oscillatory shear measurements

Oscillatory shear measurements were performed in a TA Instruments AR1000 Rheometer, using the parallel-plate shear mode to measure the storage modulus, G′, the loss modulus, G″ and the loss tangent, tan δ. The operating conditions were the following: frequency between 0.1 and 10 Hz, plate diameter 20 mm, temperature 20 °C and torque 30 μN m. The linear viscoelastic region was located with the aid of a torque sweep. All the viscoelastic measurements were performed on hydrogels swelled to equilibrium in deionized water.

2.7. Ultra small angle X-ray scattering (USAXS)

Ultra small angle X-ray scattering (USAXS) studies were performed at the ESRF's ID02 high-brilliance Beamline,[23] with a Bonse-Hart (BH) camera. The BH set-up consists of a double-crystal diffractometer. The crystals are channel-cut, and the beam bounces 3 times on them. The sample is placed between the two crystals; the second of them (analyzer) acts as an angular slit,

and it is scanned though the scattering cone of radiation. A second analyzer crystal is placed before the detector with reflection planes perpendicular to the first analyzer, in order to correct the scattering for long-slit smearing effects. The detector used was an 0-dimensional avalanche photo-diode, which recorded count values for every analyzer position.

The scattering vector is related to the scattering angle θ as $q = 4\pi \sin(\theta/2)/\lambda$, where λ is the wave-length of the incoming radiation. The analyzer crystal rocks along the θ scattering angle in a logarithmic scan. The detector follows the rocking angle accordingly.

The X-rays were produced with two undulators in tandem, by electrons at 6 GeV in the ESRF's synchrotron storage ring. The beam was focused, collimated and monochtomatized to 12.46 keV ($\lambda = 1$ Å). The total scattering vector (q) explored spans from 10^{-4} to 2.10^{-1} Å^{-1}, in the USAXS range. A set of aluminium attenuators is used to automatically control the irradiation of the sample.

The samples were kept at room temperature and constant moisture between thin Kapton™ foils in sealed aluminium sample holders. The measurements were performed in 110 intensity measurement points of 1 s exposure time, at each θ position of the crystal.

The scattering patterns were normalized to the maximum of the transmission at the sample and subtracted from the empty cuvette and the rocking curve of the crystals.

3. Results and discussion

3.1. Molecular composition of iron oxide nanoparticles

The Raman spectrum corresponding to the samples Alg0.5-PNiPAAm and FeAlg0.5-PNiPAAm (1c) are shown in Fig. 1. The main bands appearing in the Alg0.5-PNiPAAm spectrum are listed in Table 2. Based on assignments in the literature,[24,25] the bands in the Alg0.5-PNiPAAm spectrum correspond to the PNiPAAm component. No bands corresponding to alginate are observed, most likely due to the low alginate concentration of the sample with respect to the PNiPAAm component. Regarding the
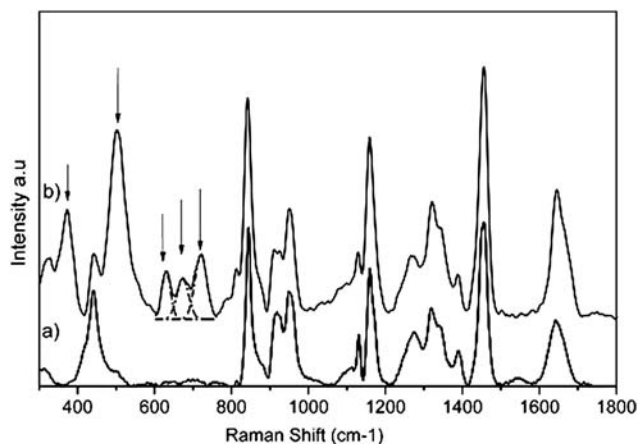

Fig. 1 Raman spectra of Alg0.5-PNiPAAm with (a) no iron oxide nanoparticles and (b) iron oxide nanoparticles. Dashed line represents the deconvolution of the peak at 700 cm^{-1}. Arrows indicate Raman bands assigned to NPs.

Table 2 Observed Raman Frequencies and assignments of the Individual Bands of Alg1-PNiPAAm spectrum

Wavenumber/cm^{-1}	Band assignment
1645	Amide I, C=O stretching
1551	Amide II, N–H bending
1455	CH$_3$ symmetric deformation
1390	CH$_3$ symmetric deformation
1340	CH deformation
1320	CH deformation
1277	CH deformation
1160	Amide III
1130	CH$_3$ rocking
845, 918,950	CC skeletal vibration

sample FeAlg0.5-PNiPAAm (1c), three new bands at 380, 502 and 630 cm^{-1} appear in the Raman spectrum in addition to the bands located at 670 cm^{-1} and at 710 cm^{-1} corresponding to magnetite and maghemite respectively.[26,27] The first two bands detected can be assigned to maghemite in good agreement with literature whereas the presence of the third band at 630 cm^{-1} is a clear indication of the formation of iron oxide hematite (α-Fe$_2$O$_3$), a potential product of magnetite oxidation.[28] It has been recently shown that the excessive exposure of magnetite to laser radiation, during a Raman measurement, can generate hematite although the required laser power threshold values differ widely since they strongly depend on operating conditions. So in order to prevent this effect, Raman spectra were taken at low laser power values and exposure times, not observing any significant variation of hematite/magnetite ratio with time. In addition, it is well established that if this iron oxide, α-Fe$_2$O$_3$, were formed during the laser exposition of magnetite occurring during the Raman experiment, the characteristic peaks of magnetite would shift to lower frequencies and the band at 670 cm^{-1} would disappear.[29] Instead, in Fig. 1, we do not observe any shift on the magnetite bands and the band at 670 cm^{-1} is very intense, thus the formation of hematite is previous to the Raman experiment. The oxidation of magnetite to hematite occurring in the sample with 0.5 wt% sodium alginate suggests that part of the iron oxide NPs formed are not effectively protected by the polymer matrix and thus they are more prone to oxidation. It is worthy of remark that recent confocal Raman experiments performed on the sample containing 1 wt% alginate and subjected to one oxidation cycle, FeAlg1-PNiPAAm (1c), only showed the simultaneous formation of magnetite, Fe$_3$O$_4$, and maghemite, γ-Fe$_2$O$_3$ and the presence of hematite, α-Fe$_2$O$_3$, was not ascertained.[20]

Raman spectra corresponding to Alg-PNiPAAm semiIPNs containing iron oxide NPs do not allow us to demonstrate the presence of interactions between the iron oxide NPs and the polymer matrix that are more likely to involve the alginate functional groups due to the low alginate concentration of the sample with respect to the PNiPAAm component. Therefore, swelling and viscoelastic measurements will be employed in order to infer the presence of these interactions and the results will be presented in the next section.

3.2. Swelling and viscoelastic properties

The water content, W_t, as a function of the iron oxide NPs volume fraction (Φ_{NPs}) is represented in Fig. 2. As can be
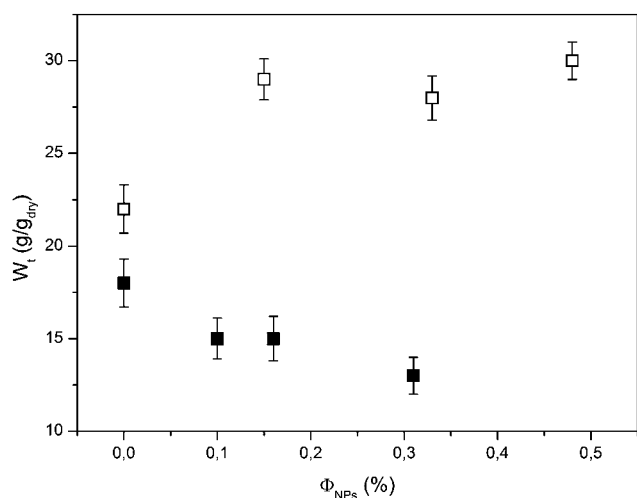
Fig. 2 Water content of swollen ferrogels as a function of the volume fraction of nanoparticles, Φ_{NPs} (%). ($\square$) Series I (0.5 wt % alginate); ($\blacksquare$) Series II (1 wt% alginate).

Fig. 3 Variation of G′ ($\blacksquare$) and G″ ($\bullet$) with oscillation frequency for Alg1-PNiPAAm and FeAlg1-PNiPAAm (1c) (open symbols).

observed, independently from the number of oxidation cycles, the water uptake is larger for samples corresponding to series I (0.5 wt% alginate). This might explain the higher iron oxide content found for these samples compared to samples corresponding to series II (1 wt% alginate) (see Table 1). In fact, the process of formation of iron oxide NPs involves the diffusion of ferrous/ferric ions into the polymer matrix and their subsequent *in situ* precipitation by an alkaline solution. This process basically depends on the swelling capacity of the hydrogel which in turn varies as a function of the chemical composition of the gel, in this case with the alginate content. Therefore it is expected that the higher the water uptake is, the more iron oxide NPs will be formed.

Fig. 2 also shows that for both series, the introduction of nanoparticles within the polymeric network strongly modifies the swelling properties. For series I (0.5 wt% alginate content), the *in situ* synthesis of iron oxide NPs increases the water uptake. This is a consequence of the large osmotic pressure that results from the difference in ionic concentration between the external solution and the bulk gel.[30] On the contrary, the presence of iron oxide nanoparticles in series II (1 wt% alginate content) entails a decrease of water uptake. Such a decrease in the total water content, might be attributed to effective interactions between the NPs and the polymer matrix.[31] These interactions may arise from the alginate carboxylic groups that would act as iron-binding and later oxidation sites of iron cations to iron oxide nanoparticles.[32] Taking into account that the number of carboxylic groups is double and the iron oxide NPs volume fraction is lower in series II than in series I, it could be hypothesized that for series II most of the iron oxide NPs interact with the polymer matrix.[33,34]

In order to indirectly verify the proposed interactions between the polymer matrix and the iron oxide nanoparticles, oscillatory shear measurements were carried out on swollen hydrogels of series I and II. As a representative example, Fig. 3 shows the elastic and the loss modulus obtained for the sample Alg1-PNiPAAm and FeAlg0.5-PNiPAAm (1c) as a function of frequency. To be considered a gel, the system must meet some requirements according to its rheological behaviour:[35] (i) its dynamic elastic
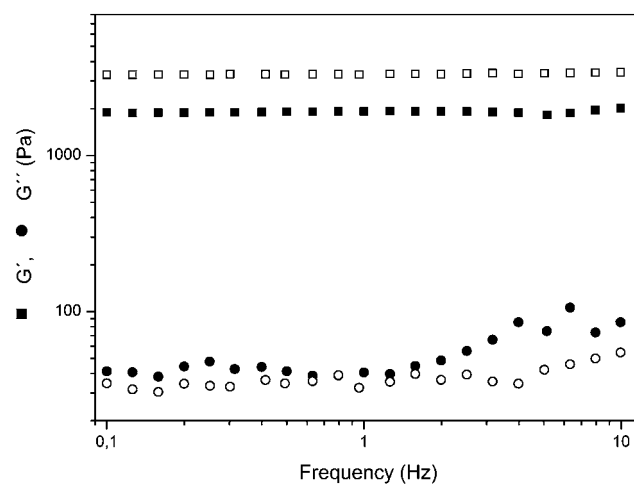
modulus (G′) must be relatively independent of the frequency of deformation and (ii) G′ must be greater than G″ at all frequencies. These two characteristics are observed in Fig. 3 where both samples present a gel-like behaviour at $T = 20$ °C which is characterized by the frequency-independence of G′ and G″, being G′ higher than G″ at all frequencies. In addition, the elastic modulus, G′ corresponding to the sample FeAlg1-PNiPAAm (1c) containing iron oxide nanoparticles is higher than the elastic modulus, G'_0 of the sample Alg1-PNiPAAm without iron oxide NPs. Therefore, the introduction of iron oxide NPs reinforces the polymeric matrix mechanically as reported for other polymeric matrixes with colloidal nanoparticles.[36–38]

The reinforcement factor (G'/G'_0) as a function of the iron oxide NPs volume fraction for series I and series II is depicted in Fig. 4. As can be observed, for both series, the reinforcement of the network induced by the introduction of iron oxide NPs increases with the volume fraction of iron oxide NPs in the gel. Nevertheless, the ratio (G'/G'_0) increases much more sharply for
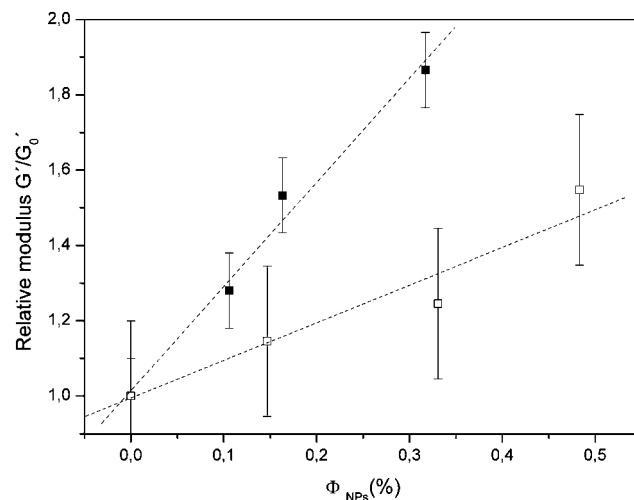
Fig. 4 Reinforcement G'/G'_0 of ($\square$) Series I (0.5 wt% Alg) and ($\blacksquare$) Series II (1 wt% Alg) as a function of the volume fraction of nanoparticles.

the samples corresponding to series II than for the samples corresponding to series I. In fact, the slope obtained from the linear fitting of the plot corresponding to series I yields a slope of 1.06 ± 0.54, which is ~2.5-fold lower than the corresponding to the samples of series II (slope = 2.76 ± 0.43).

In series I this result would indicate the absence of an effective interface between the polymer matrix and the iron oxide nanoparticles suggesting the lack of effective interactions between them as previously demonstrated through swelling experiments. In fact, as it is widely reported, the establishment of interactions between nanoparticles and the polymer matrix greatly influences the mechanical properties of filled polymers.[39-41] In this sense, samples corresponding to series II (1 wt% alginate) seem to present a better adhesion of the filler particles with the polymer matrix and hence the presence of interactions can be inferred.

In order to gain further insight into the relationship between the NPs content and the reinforcement of the ferrogels, we compared the experimental values represented in Fig. 4 with the values predicted by the well known Einstein equation:[42]

$$G'(\Phi) = G'_0 (1 + 2.5\,\Phi) \tag{3}$$

This equation was initially derived to explain the viscosity of suspensions of rigid spherical inclusions but it can be employed for composite systems, mainly elastomers[43] and to model the reinforcement of elastic modulus in ferrogels due to filler particles.[37] Eqn (3) is valid for rigid spherical particles at small concentrations, under the assumption that there is perfect adhesion at the interface and the properties of each phase are everywhere identical to those in the bulk. We found that the values predicted by eqn (3) for the ratio (G'/G'_0) underestimates the experimental values depicted in Fig. 4 which might be due to the presence of aggregates as demonstrated for other nanocomposite polymer systems[44] and that it will be demonstrated for our systems later on through USAXS experiments.

3.3. Structural organization

In order to investigate the structure exhibited by iron oxide nanoparticles, USAXS measurements were carried out.

Fig. 5 shows the scattering patterns of samples corresponding to series I (0.5 wt% alginate) along with a representative transmission electron microscopy (TEM) image corresponding to the dried sample FeAlg0.5-PNiPAAm (1c). The scattering patterns of samples corresponding to series II (1 wt% alginate) are depicted in Fig. 6. The insert in this figure shows a representative TEM image corresponding to the dried sample FeAlg1-PNiPAAm (1c). Interestingly, none of the samples under study present a scattering peak which indicates the absence of interactions between aggregates.[44]

Porod and Guinier regimes can be combined in a single equation which describes the scattering, $I(q)$ of any morphology containing a random distribution of structure:[45,46]

$$I(q) = G\exp(-q^2 R_g^2/3) + B\{[erf(qR_g/6^{1/2})]^3/q\}^P \tag{4}$$

where G and B are exponential prefactors, R_g is the radius of gyration, erf is the error function and P is the Porod exponent. Eqn (4) can be extended to describe an arbitrary number of
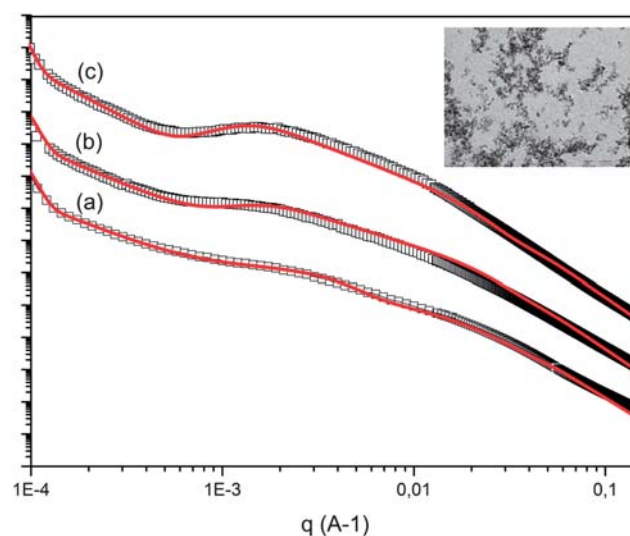

Fig. 5 Scattered intensity I as a function of scattering wave vector q in $\mathring{A}^{-1}$ from ferrogels corresponding to **series I** (0.5 wt% alginate) subjected to a varying number of cycles (a) 1c; (b) 2c; (c) 3c. The solid line represents the fitting to the unified model. The insert shows a representative TEM image corresponding to the sample FeAlg0.5-PNiPAAm (1c).

Fig. 6 Scattered intensity I as a function of scattering wave vector q in $\mathring{A}^{-1}$ from ferrogels corresponding to **series II** (1 wt% alginate) subjected to a varying number of cycles (a) 1c; (b) 2c; (c) 3c. The solid line represents the fitting to the unified model. The insert shows a representative TEM image corresponding to the sample FeAlg1-PNiPAAm (1c).
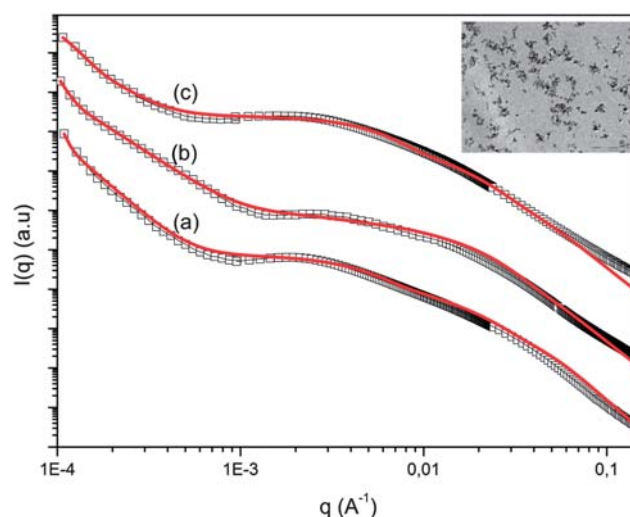
interrelated structural levels, known as the unified model[45,47] according to:

$$I(q) \approx \sum_{i=1}^{n} \left(G_i \exp\left(-q^2 R_{g_i}^2/3\right) + B_i \exp\left(-q^2 R_{g_{(i+1)}}^2/3\right) \right. \\ \left. \times \left\{ \left[erf\left(q R_{g_i}/6^{1/2}\right) \right]^3 / q \right\}^{P_i} \right) \tag{5}$$

where $i = 1$ refers to the largest-size structural level. In our case we can consider $i = 1$ as a large structure contributing to the excess of scattering at low q-values, corresponding to the

agglomerates formation, the next level of structure, $i = 2$, would correspond in our case to the structural parameters corresponding to the aggregates. Last, a third structural parameter $i = 3$ would correspond to the scattering of primary iron oxide NPs.

The scattering data corresponding to series I and II are well-described by the unified fit as can be observed in Fig. 5 and 6. As a representative example, Fig. 7 shows the component curves of the global unified fit for the sample FeAlg0.5-PNiPAAm(1c). At high q ($q > 0.03$ Å^{-1}), the scattered intensity decays following a power-law (Porod's law ($I(q) = B_{porod}q^{-4}$). The Porod exponent, P is ~ 4 for all the samples under study which indicates that the iron oxide NPs develop smooth and sharp interfaces with the polymer matrix (dashed line). This first power-law (Porod regime) is followed at lower q by a knee-like decay (Guinier regime) (dotted lines). This knee-like decay in intensity reflects the structural size of primary particles. The scattering for this regime follows Guinier's law:

$$I(q) = G\exp(-q^2 R_g^2/3) \tag{6}$$

where G is the Guinier prefactor and R_g is the radius of gyration. A second Guinier regime can be plotted that reflects the size of the aggregates. From eqn (6), the radius of gyration of the primary particles, R_{g3} and the radius of gyration of the aggregates, R_{g2} can be derived. The slope of the weak power-law decay between the two Guinier knees is directly related to the mass fractal structure of the aggregates by:

$$I(q) = B_2 q^{-Df} \tag{7}$$

where D_f is the mass-fractal dimension and B_2 is the law prefactor. A third power-law regime is shown at $q < 10^{-3}$ Å^{-1} which describes agglomerates. For this structural level, the upturn at $q < 2 \times 10^{-4}$ Å^{-1} is well fitted by considering the contribution of the radius of gyration of the agglomerates, R_{g1} according to eqn (6). However, the q range is not wide enough for the appropriate study of this larger structure.
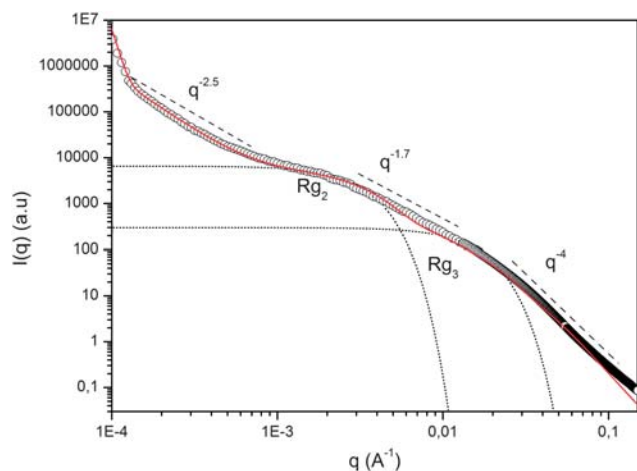

Fig. 7 Scattered intensity I as a function of scattering wave vector q in Å^{-1} for sample FeAlg0.5-PNiPAAm (1c) (open circles). Unified fit (solid line) and Guinier regimes (dotted lines). Additional dashed lines are included to guide the reader's attention.

Table 3 Power law exponents for the two series under consideration determined from least-squares fits to the scattering data shown in Fig. 5 and 6

	Number of oxidation cycles	High-q power law exponent (D_f mass fractal)	Low-q power law exponent (Porod agglomerates)
Series I (0.5 wt% alginate)	1c	-1.74 ± 0.02	-2.48 ± 0.06
	2c	-1.81 ± 0.02	-2.57 ± 0.07
	3c	-1.91 ± 0.03	-2.61 ± 0.07
Series II (1 wt% alginate)	1c	-1.70 ± 0.01	-4.09 ± 0.08
	2c	-1.16 ± 0.03	-3.30 ± 0.03
	3c	-1.81 ± 0.02	-3.45 ± 0.09

Table 3 shows the power law exponents for the different structural regimes exhibited by the iron oxide nanoparticles inside the Alg-PNiPAAm semi-IPNs determined from least-squares fits to eqn (5) for the scattering data shown in Fig. 5 and 6. Regarding the mass-fractal dimension, D_f, for both series it increases from -1.74 to -1.91 when the number of oxidation cycles is increased from 1 to 3. These values confirm that the primary particles are organized into fractals and that the structure is more compact as the iron oxide NPs volume fraction increases. No appreciable differences are obtained between both series which suggest that the primary particle organization in fractal structures does not depend on the alginate content. On the contrary, a big difference is observed when low-q power law exponents, that is to say the fractal exponent corresponding to agglomerates are compared for both series. The exponents obtained for samples corresponding to series I (0.5 wt% alginate content) lay between $\sim 2.48 \pm 0.06$ and 2.61 ± 0.07. Meanwhile, low-q power law exponents obtained for samples corresponding to series II (1 wt% alginate content) varies from -4.09 ± 0.08 to -3.45 ± 0.09 as the number of oxidation cycles, and hence, the iron oxide volume fraction increases. From these values, it can be inferred the existence of compact agglomerates not exhibiting a fractal structure in the case of samples corresponding to series II. Instead, the low-q power law exponents exhibited by samples corresponding to series I, with values ~ 2.48–2.61 are characteristic of fractal structures. This fractal character could result from the presence of larger agglomerates exhibiting rougher surfaces or else, from the processes of oxidation taking place during the reaction conditions as determined through confocal Raman spectroscopy.

From the determination of the fractal dimension of the aggregates, the aggregation number N_{agg} can be extracted as follows:

$$N_{agg} = \left(\frac{R_{agg}}{R_{NPs}}\right)^{D_f} \tag{8}$$

where R_{agg} and R_{NPs} denote the radius of the aggregate and of the iron oxide NPs, respectively and D_f the fractal dimension.[48] The values of R_{NPs} where obtained from Guinier plot, Ln $I(q)$ vs. q^2 and constitute a fixed parameter in equation. R_{agg} is a parameter extracted from the fitting to eqn (5). By assuming the particle shape to be a sphere, the diameter of the particle D is calculated by:[49]

$$D = 2 \times (5/3)^{1/2} R_g \tag{9}$$

Table 4 Results from the fitting to eqn (5)

	Number of oxidation cycles	D_{NPs}/nm[a]	D_{agg}/nm[b]	N_{agg}
Series I	1c	20.7 ± 0.4	133.5 ± 11.4	26
(0.5 wt% alginate)	2c	21.2 ± 0.4	473.0 ± 11.4	277
	3c	21.9 ± 0.5	547.4 ± 11.4	466
Series II	1c	19.1 ± 0.4	103.3 ± 14.4	18
(1 wt% alginate)	2c	20.6 ± 0.4	129.1 ± 12.4	8
	3c	20.9 ± 0.4	87.8 ± 12.7	13

[a] Fixed parameter obtained from Ln $I(q)$ vs. q^2 plot. [b] From fitting to eqn (5).

For polydisperse spheres, the standard deviation can be obtained directly from the three unified fit parameters, so that:[50]

$$Ln\sigma_g = \sigma = \left(\frac{Ln\left[B(R_g^2)^2/(1.62G)\right]}{12} \right)^{1/2} \quad (10)$$

Table 4 shows the obtained values for D_{agg}, D_{NPs} and N_{agg}. As can be observed, D_{NPs} extracted from the Guinier radius, do not depend either on the application of oxidation cycles nor on the alginate content and for all the samples a value around 20 nm is obtained. Differences between both series arise when D_{agg} corresponding to both series are compared. In the case of samples of series I (0.5 wt%), D_{agg} increases with the iron oxide volume fraction, and hence with the repetition of oxidation cycles, therefore, the aggregation number increases from 26 in the sample subjected to one cycle to 466 in the sample subjected to three oxidation cycles. By contrast, D_{agg} does not change appreciably in the case of samples of series II (1 wt%). This is reflected in the aggregation number that remains almost constant with the oxidation cycles. These results shows that in the case of samples of series II (1 wt% alginate), the application of oxidation cycles results in an increase of the number of aggregates without changing their size whereas in the case of samples of series I (0.5 wt% alginate), it results in an increase of the size of aggregates.

4. Conclusions

Iron oxide NPs were synthesized *in situ* by using semi-interpenetrating polymer networks of alginate and poly (*N*-isopropylacrylamide) as templates for the reaction of oxidation of iron cations in alkaline media. The analysis of the iron oxide NPs molecular structure by means of confocal Raman spectroscopy revealed the formation of hematite, formed by oxidation of magnetite which occurred previous to the Raman experiment in samples with a 0.5 wt% alginate content. On the contrary, iron oxide NPs synthesized in semi-IPNs with a 1 wt% alginate content were found to be a mixture of magnetite and maghemite. These results indicated that the iron oxide nanoparticles synthesized in semi-IPNs with lower alginate content were more prone to oxidation. Independently from the number of oxidation cycles, the amount of iron oxide NPs was found to be higher for the samples with lower alginate content which was attributed to the higher water uptake observed for these samples.

Analysis of the results showed that for samples with a 1 wt% alginate content, the establishment of effective interactions between the polymer matrix and the iron oxide NPs prevents on the one hand their oxidation and, on the other hand, induces a larger reinforcement of the network. USAXS experiments proved the absence of large aggregates for these samples and that their size does not vary with the repetition of oxidation cycles. On the contrary, the low reinforcement induced by the presence of iron oxide NPs synthesized inside semi-IPNs with a 0.5 wt% alginate content determined through rheological measurements suggests that for these samples, iron oxide NPs are simply 'packed' into the polymer matrix without interaction with the polymer matrix. As a consequence, the formation of larger aggregates is favored and the aggregation number increases with the number of oxidation cycles.

Acknowledgements

References

1 C. Echeverria and C. Mijangos, *Macromol. Rapid Commun.*, 2010, **31**, 54–58.
2 R. Mezzenga and J. Ruokolainen, *Nat. Mater.*, 2009, **8**, 926–928.
3 R. Hernandez, G. Lopez, D. Lopez, M. Vazquez and C. Mijangos, *J. Mater. Res.*, 2007, **22**, 2211–2216.
4 D. Lopez, I. Cendoya, F. Torres, J. Tejada and C. Mijangos, *Polym. Eng. Sci.*, 2001, **41**, 1845–1852.
5 D. G. Shchukin, J. H. Schattka, M. Antonietti and R. A. Caruso, *J. Phys. Chem. B*, 2003, **107**, 952–957.
6 C. R. Mayer, V. Cabuil, T. Lalot and R. Thouvenot, *Adv. Mater.*, 2000, **12**, 417–420.
7 M. Breulmann, S. A. Davis, S. Mann, H. P. Hentze and M. Antonietti, *Adv. Mater.*, 2000, **12**, 502–507.
8 R. Tannenbaum, M. Zubris, E. P. Goldberg, S. Reich and N. Dan, *Macromolecules*, 2005, **38**, 4254–4259.
9 Y. Wang, B. Li, Y. Zhou and D. Jia, *Polym. Adv. Technol.*, 2008, **19**, 1256–1261.
10 A. L. Daniel-da-Silva, T. Trindade, B. J. Goodfellow, B. F. O. Costa, R. N. Correia and A. M. Gil, *Biomacromolecules*, 2007, **8**, 2350–2357.
11 A. Haug, B. Larsen and O. Smidsrod, *Acta Chem. Scand.*, 1966, **20**, 183–183.
12 Y. Nishio, A. Yamada, K. Ezaki, Y. Miyashita, H. Furukawa and K. Horie, *Polymer*, 2004, **45**, 7129–7136.
13 E. Kroll, F. M. Winnik and R. F. Ziolo, *Chem. Mater.*, 1996, **8**, 1594–1596.
14 H.-l. Ma, X.-r. Qi, Y. Maitani and T. Nagai, *Int. J. Pharm.*, 2007, **333**, 177–186.
15 Jian Qin, I. Asempah, S. Laurent, A. Fornara, R. N. Muller and M. Muhammed, *Adv. Mater.*, 2009, **21**, 1354–1357.
16 V. M. De Paoli, S. H. De Paoli Lacerda, L. Spinu, B. Ingber, Z. Rosenzweig and N. Rosenzweig, *Langmuir*, 2006, **22**, 5894–5899.
17 T.-Y. Liu, S.-H. Hu, T.-Y. Liu, D.-M. Liu and S.-Y. Chen, *Langmuir*, 2006, **22**, 5974–5978.
18 N. S. Satarkar and J. Z. Hilt, *J. Controlled Release*, 2008, **130**, 246–251.
19 T.-Y. Liu, S.-H. Hu, K.-H. Liu, D.-M. Liu and S.-Y. Chen, *J. Controlled Release*, 2008, **126**, 228–236.
20 R. Hernández, J. Sacristán, A. Nogales, T. A. Ezquerra and C. Mijangos, *Langmuir*, 2009, **25**, 13212–13218.
21 K. J. Sreeram, H. Yamini Shrivastava and B. U. Nair, *Biochim. Biophys. Acta, Gen. Subj.*, 2004, **1670**, 121–125.
22 F. Llanes, D. H. Ryan and R. H. Marchessault, *Int. J. Biol. Macromol.*, 2000, **27**, 35–40.
23 M. Sztucki, J. Gorini, J.-P. Vassalli, L. Goirand, P. van Vaerenbergh and T. Narayanan, *J. Synchrotron Radiat.*, 2008, **15**, 341–349.
24 Y. Maeda, T. Higuchi and I. Ikeda, *Langmuir*, 2000, **16**, 7503–7509.
25 Y. Maeda, H. Yamamoto and I. Ikeda, *Macromolecules*, 2003, **36**, 5055–5057.

26 K. Herve, L. Douziech-Eyrolles, E. Munnier, S. Cohen-Jonathan, M. Souce, H. Marchais, P. Limelette, F. Warmont, M. L. Saboungi, P. Dubois and I. Chourpa, *Nanotechnology*, 2008, **19**, 465608.

27 S.-H. Hu, T.-Y. Liu, D.-M. Liu and S.-Y. Chen, *J. Controlled Release*, 2007, **121**, 181–189.

28 I. Chourpa, L. Douziech-Eyrolles, L. Ngaboni-Okassa, J.-F. Fouquenet, S. Cohen-Jonathan, M. Souce, H. Marchais and P. Dubois, *Analyst*, 2005, **130**, 1395–1403.

29 O. N. Shebanova and P. Lazor, *J. Solid State Chem.*, 2003, **174**, 424–430.

30 J. A. Galicia, F. Cousin, E. Dubois, O. Sandre, V. Cabuil and R. Perzynski, *Soft Matter*, 2009, **5**, 2614–2624.

31 K. Christodoulakis, D. Palioura, S. Anastasiadis and M. Vamvakaki, *Top. Catal.*, 2009, **52**, 394–411.

32 E. Torres, Y. N. Mata, M. L. Blazquez, J. A. Munoz, F. Gonzalez and A. Ballester, *Langmuir*, 2005, **21**, 7951–7958.

33 M. M. Figueira, B. Volesky and H. J. Mathieu, *Environ. Sci. Technol.*, 1999, **33**, 1840–1846.

34 K. J. Sreeram, M. Nidhin and B. U. Nair, *Colloids Surf., B*, 2009, **71**, 260–267.

35 G. M. Kavanagh and S. B. Ross-Murphy, *Prog. Polym. Sci.*, 1998, **23**, 533.

36 J. A. Galicia, O. Sandre, F. Cousin, D. Guemghar, C. Ménager and V. Cabuil, *J. Phys.: Condens. Matter*, 2003, **15**, S1379–S1402.

37 R. Hernández, A. Sarafian, D. López and C. Mijangos, *Polymer*, 2004, **45**, 5543–5549.

38 J. Oberdisse, P. Hine and W. Pyckhout-Hintzen, *Soft Matter*, 2007, **3**, 476–485.

39 F. Sahnoune, J. M. Lopez-Cuesta and A. Crespy, *J. Mater. Sci.*, 1999, **34**, 535–544.

40 S. Guhanathan and M. S. Devi, *J. Appl. Polym. Sci.*, 2005, **97**, 171–184.

41 M. A. López-Manchado, J. L. Valentín, J. Carretero, F. Barroso and M. Arroyo, *Eur. Polym. J.*, 2007, **43**, 4143–4150.

42 A. Einstein, *Investigation on theory of Brownian motion*, Dover, New York, 1956.

43 G. Heinrich, M. Klüppel and T. A. Vilgis, *Curr. Opin. Solid State Mater. Sci.*, 2002, **6**, 195–203.

44 J. Oberdisse, *Macromolecules*, 2002, **35**, 9441–9450.

45 G. Beaucage, *J. Appl. Crystallogr.*, 1995, **28**, 717–728.

46 J. Teixeira, *J. Appl. Crystallogr.*, 1988, **21**, 781–785.

47 K. K. Hendrik, B. Gregory, J. K. Douglas, A. Nikhil and I. Jan, *J. Appl. Phys.*, 2005, **97**, 054309.

48 J. Oberdisse, A. El Harrak, G. Carrot, J. Jestin and F. Boue, *Polymer*, 2005, **46**, 6695–6705.

49 K. Hino, R. Shingai, T. Morita, K. Toku, T. Hirano, H. Yoshikawa, H. Nakano and N. Nishi, *Chem. Phys. Lett.*, 2008, **460**, 173–177.

50 G. Beaucage, H. K. Kammler and S. E. Pratsinis, *J. Appl. Crystallogr.*, 2004, **37**, 523–535.